Locomotion of magnetoelastic membranes in viscous fluids

Chase Austyn Brisbois

Department of Materials Science and Engineering, Northwestern University, Evanston, IL 60208, USA

Monica Olvera de la Cruz [*]

Department of Materials Science and Engineering, Northwestern University, Evanston, IL 60208, USA;
Department of Chemistry, Northwestern University, Evanston, IL 60208, USA;
and Department of Physics and Astronomy, Northwestern University, Evanston, IL 60208, USA

The development of multifunctional and biocompatible microrobots for biomedical applications relies on achieving controllable locomotion. Here we describe the conditions that allow homogeneous magnetoelastic membranes composed of superparamagnetic particles to swim through viscous fluids. By solving the equations of motion, we find the dynamical modes of circular membranes in precessing magnetic fields, which are found to actuate in or out of synchronization with a magnetic field precessing above or below a critical precession frequency ω_c, respectively. For frequencies larger than ω_c, synchronized transverse waves propagate on the membrane along the rotational (perimeter) and radial directions. Using the lattice Boltzmann approach, we show how these waves give rise to locomotion in an incompressible fluid at low Reynolds numbers. Nonreciprocal motion resulting in swimming is achieved by breaking the morphological symmetry of the membrane, attained via truncation of a circular segment. The membrane translation can be adapted to a predetermined path by programming the external magnetic field. Our results lay the foundation for achieving directed motion in thin, homogeneous magnetoelastic membranes with a diverse array of geometries.

I. INTRODUCTION

Magnetically controlled microrobots have applications in drug delivery [1–4], sensing [5–7], micromixing [8], detoxification [9,10], and microsurgery [11,12]. Such versatile use of magnetic microrobots is possible because magnetic fields can penetrate organic matter, do not interfere with biological or chemical functions, can replace chemical fuels that drive robotic actuation, and, most importantly, can be externally controlled. These properties allow for noninvasive and precise spatiotemporal execution of desired function. Superparamagnetic particles, in particular, are ideal candidates for robotic functions because they lack residual magnetization, which lowers their propensity to agglomerate, and they are less toxic than ferromagnetic particles [13]. When linked along a linear elastic chain, they form magnetoelastic filaments that bend and swim in response to time-dependent magnetic fields [2,14]. While filaments possess a repertoire of possible actuating modes, magnetoelastic membranes [15,16] combine the functionality of 1D filaments, such as their high surface area-to-volume ratio and ability to swim, with the function-

ality of 3D magnetic gels, such as encapsulation and tunable porosity [17]. Using 2D patterning methods, membranes possess unique shape-transforming properties that allow them to dynamically switch between functional states [18,19], making membranes highly suited for designing multifunctional microrobots.

Nonreciprocal motion induced via competing magnetic and elastic interactions is required for microscopic, magnetoelastic robots to navigate viscous environments [20]. That is, the sequence of configurations that the robot adopts must break time-reversal symmetry to swim at low Reynolds numbers (Re $= vL/\nu \ll 1$ where L and v are the length and speed of the robot, respectively, and ν is the kinematic viscosity of the fluid). Under these conditions, inertia is negligible. Hence a microrobot in water experiences the same difficulty that a sardine may experience trying swim in peanut butter (Re $\sim 10^{-3}$), that is, reciprocal back-and-forth motion will not produce swimming [21]. Magnetoelastic filaments achieve nonreciprocal motion with a nonhomogeneous distribution of magnetic components or with shape asymmetry [2–4,22,23]. In these previous studies, asymmetries in magnetic filaments induce bending waves that propagate along the filament, resulting in propulsion.

In nature, microscopic organisms such as euglenids swim using self-propagating waves directed along their cellular membrane [24]. G. I. Taylor was the first to model such organisms using a transverse wave traveling along an infinite 2D sheet [25]. Taylor found that the wave induced motion in the sheet opposite to the propagating wave direction. Subsequent

---

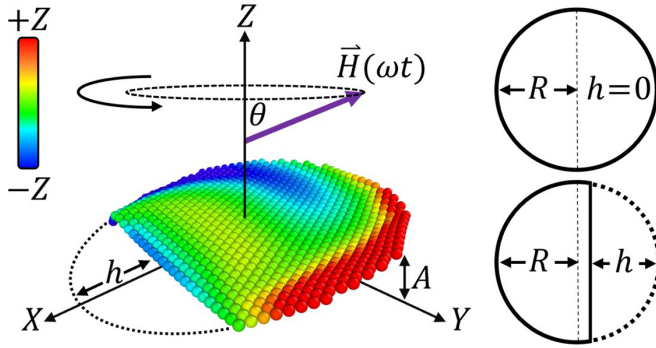[*]m-olvera@northwestern.edu

023166-1

FIG. 1. An image of a truncated magnetoelastic membrane in a precessing magnetic field. The degree of truncation $S = h/2R$, where h is the sagitta length of the removed circular segment, and R is the membrane radius, determines membrane symmetry. The magnetic field $\vec{H}$ precesses at the angle θ around the z axis with a phase given by $\phi = \omega t$, where ω is the precession frequency and t is time. The field induces a transverse wave along the membrane perimeter with amplitude A, measured from the x-y plane. Coloration indicates the z position as shown by the color bar on the left.

works expanded on Taylor's findings [26] and developed a rotational counterpart [27] that produces a hydrodynamic torque on circular membranes with prescribed waves traveling around their perimeter.

In this article, we study rotational waves in homogeneous magnetoelastic membranes under precessing magnetic fields. The membrane is composed of hexagonally packed, superparamagnetic colloids that are bonded to their nearest neighbors. Similarly to magnetoelastic filaments [6,7], the bonding between colloids makes the membrane inextensible but able to elastically bend. We investigate the dynamic modes of these membranes that are separated by a critical precession frequency ω_c, below which the membrane motion is asynchronous with the field and above which rotational waves propagate in-phase with the field precession. Breaking the membrane's center of inversion symmetry by removing part of the circle [Fig. 1] allows for locomotion in the fast frequency phase ($\omega > \omega_c$). Shape asymmetry is needed to disrupt the inversion symmetry of the magnetic forces experienced by a circular membrane. We show that the torque and velocity of the membrane counterintuitively resemble the linear Taylor sheet rather than its rotational analogue. Furthermore, by controlling a magnetoviscous parameter and the membrane shape asymmetry, we demonstrate swimming directed by a programmed magnetic field and diagram its nonreciprocal path through conformation space.

The paper is organized as follows. In Sec. II, we establish the phase diagram of a circular magnetoelatic membrane in a precessing magnetic field and determine the transition frequency ω_c. In Sec. III, we introduce hydrodynamic interactions and observe circular locomotion in asymmetric membranes. We demonstrate a programmed magnetic field, in Sec. IV, that directs a membrane swimmer along a predetermined path. Finally, we make concluding remarks on the necessary conditions for superparamagnetic swimmers in Sec. V.

II. PHASE SPACE FOR UNTRUNCATED MEMBRANE

We construct the phase diagram for the dynamic modes of the membrane using molecular dynamics (MD) without hydrodynamics to efficiently search for nonreciprocal actuation relevant to locomotion. Actuation of magnetoelastic membranes in time-dependent magnetic fields necessitates a model that captures elastic bending in response to magnetic forces, which are imparted by the dipolar interactions of embedded magnetic colloids. The membrane is composed of a hexagonal close-packed monolayer of hard spherical colloids, each of diameter σ and possessing a point dipole moment $\boldsymbol{\mu}$ at its center. The bonds between the colloids are approximately inextensible but able to bend with rigidity κ. The energy scale for κ is given by the energy unit ϵ.

We model an implicit, uniform magnetic field by constraining the orientation of the colloids' dipole moments in the direction of the field, $\boldsymbol{H} = \boldsymbol{\mu}/\chi$, where χ is the magnetic susceptibility of the material and $\boldsymbol{\mu}$ is the dipole moment with magnitude μ. The instantaneous dipole orientation is given by $\hat{\boldsymbol{\mu}} = \sin\theta \sin\omega t\, \hat{\boldsymbol{i}} + \sin\theta \cos\omega t\, \hat{\boldsymbol{j}} + \cos\theta\, \hat{\boldsymbol{k}}$, where θ is the field precession angle, ω is the precession frequency, and t is time. The scale for t and ω^{-1} is given in units of $t^* = \sigma\sqrt{m/\epsilon}$, where m is the mass of a colloid, and the dipole μ is reported in units of $\sqrt{\mu_0/4\pi\sigma^3\epsilon}$, where μ_0 is the magnetic permeability.

A diverse set of possible actuations develops depending on the radius R of the thin membrane and the magnetic field parameters (μ, θ, ω). While varying these parameters, we solve the equations of motion for an overdamped system with a friction force imparted on each colloid given by $-\xi\boldsymbol{v}(t)$, where $\boldsymbol{v}(t)$ is the colloid velocity, and ξ is the damping coefficient. See Appendix A for more details on the MD model.

Within this approximation, two dynamic mode regimes develop. At fast frequencies ($\omega > \omega_c$), the membrane motion synchronizes with the field to produce transverse waves that propagate around the membrane [Fig. 2(a)]. We refer to these membranes as "wobblers." At slow frequencies ($\omega < \omega_c$), we observe a collection of modes that are asynchronous with the field resulting in membrane "dancers" that periodically buckle and spin. The actuation modes of these two regimes are separated by a critical frequency, ω_c [Fig. 2(b)].

As the field precesses, the forces along the membrane perimeter generate internal buckling and create a torque that rotates the membrane around its diameter. If the magnetic field precession is fast ($\omega > \omega_c$), the continuous change in the direction of the axis of rotation leads to the development of a constant-amplitude wave traveling along the membrane perimeter; see Supplemental Material for Video 1 in Ref. [28]. On average, the membrane remains perpendicular to the precession axis and simply "wobbles," synchronous to the field, and with no significant rotation around the precession axis. This state closely resembles acoustically levitated granular rafts [29].

The direction of the propagating wave matches the handedness of precession because the dipole-dipole forces, which cause buckling, point in the direction of the magnetic field. However, the field polarity does not affect the magnitude or travel direction of the wave since the superparamagnetic dipoles are always oriented in the same direction as the field.
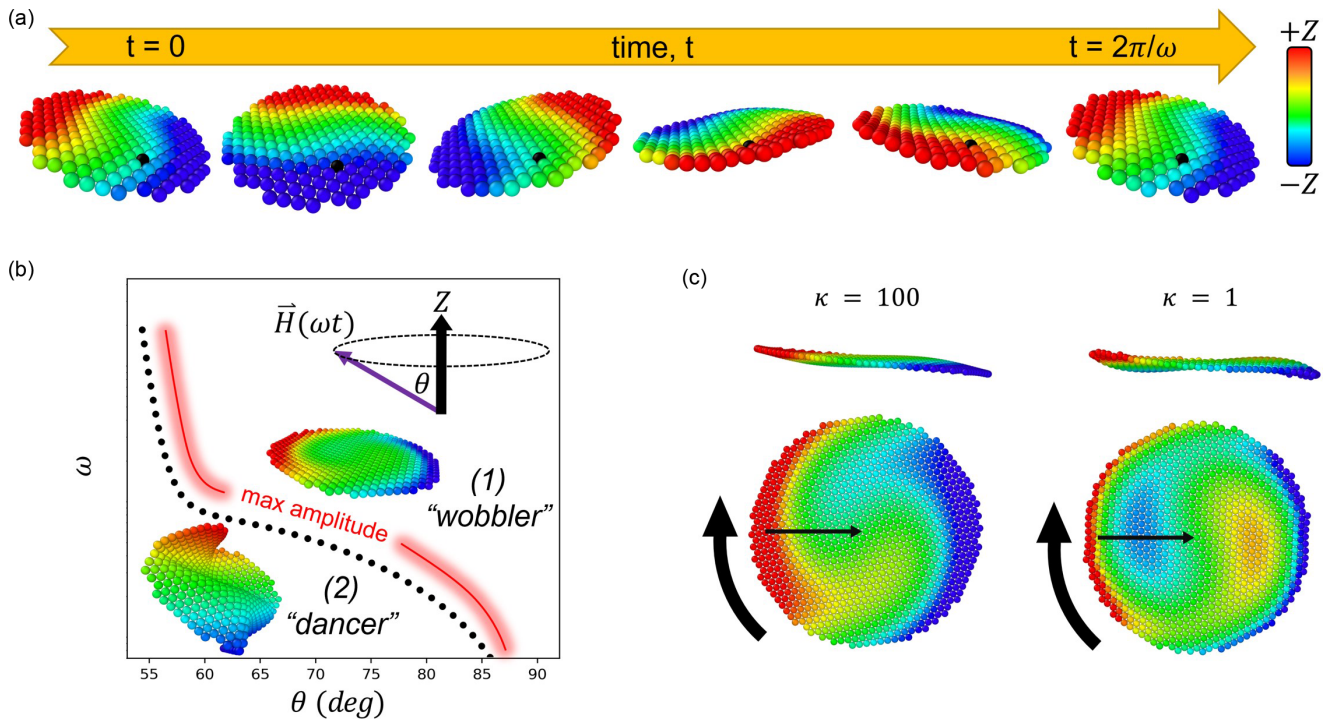
FIG. 2. A circular magnetoelastic membrane in a precessing magnetic field. (a) Transverse waves propagate around the membrane above a critical frequency ($\omega > \omega_c$) with negligible membrane rotation highlighted by the black-colored colloid. Coloration indicates the z position as shown by the color bar in the top right corner. (b) A schematic plot showing the phase diagram of a membrane. Above the dotted black curve, the "wobbling" membrane remains perpendicular to the precession axis and possess the rotational waves from (a). The wave amplitude maximizes just before the transition. Below this curve, the membrane buckles and rotates asynchronously with the field, hence "dancers." (c) The bending stiffness controls the shape of the rotational waves. The black arrows indicate the direction of wave propagation along the perimeter (thick arrow) and radially toward the membrane center (thin arrow).

Hence the force due to the dipole-dipole interactions $\boldsymbol{F}_\text{dipole}$ remains unchanged ($\boldsymbol{F}_\text{dipole} \propto (\boldsymbol{\mu} \cdot \boldsymbol{r})\boldsymbol{\mu} = (-\boldsymbol{\mu} \cdot \boldsymbol{r})(-\boldsymbol{\mu})$, where $\boldsymbol{r}$ is the displacement vector between dipoles [30]).

In addition to the rotational waves, the wobbling mode also manifests radially propagating (inward) bending waves [Fig. 2(c)] that terminate at the membrane center. The wave shape weakly depends on the membrane stiffness κ; the wave form is better defined as κ decreases. However, totally compliant membranes ($\kappa \to 0$) do not transmit bending waves and therefore this phenomenon exists only for intermediate κ.

If the precession is slow ($\omega < \omega_c$), the membrane has enough time to rotate completely parallel to the precession axis and will adopt new configurations due to elastic buckling. How the membrane buckles depends on the magnetoelastic parameter [15] $\Gamma = ML^2/\kappa$, which characterizes the ratio between the membrane's magnetic and bending energies, where M is the magnetic modulus, and L^2 is the membrane area. If the magnitude of Γ is very small ($\Gamma \ll 1$) or very large ($\Gamma \gg 1$), we observe hard disk behavior because bending distortions become impossible due to mechanical stiffness or due to unfavorable magnetic interactions, respectively. While not investigated here, strong magnetic coupling [31,32] between colloids will adversely affect membrane synthesis.

At intermediate Γ, membrane edges buckle several times per precession period and produce magnetically stabilized conformations that, while periodic, run out of sync with the field; see Supplemental Material for Video 2 in Ref. [33].
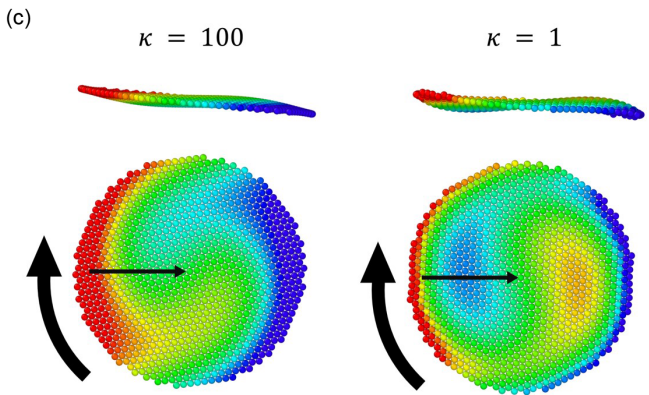
Much of this back-and-forth "dancing" motion is essentially reciprocal and is, therefore, a poor candidate for studying swimming at small Re. Subsequently, we seek to formally define ω_c and focus on the wobbling regime ($\omega > \omega_c$).

To accurately determine the transition frequency ω_c that separates the wobblers from the dancers, we investigate how the magnetic field parameters (precession angle θ, dipole magnitude μ) and membrane radius R, in units of σ [Fig. 3(a)], contribute to the characteristic response time τ of the rotating membrane. When the membrane rotation time τ increases, it necessarily requires a slower field to keep the membrane in the wobbling mode, decreasing ω_c. A larger τ can be achieved by weakening the magnetic torque (θ closer to $\pi/2$ or smaller μ) or increasing the drag on the membrane (larger R). Similarly, a smaller τ implies a fast membrane response from a strong field or a small membrane. We observe that ω_c diverges as θ approaches the magic angle, partly due to instability of the wobbling phase at angles below the magic angle [34].

The transition to the wobbling state is characterized by the abrupt shift in the membrane's total potential energy U, given in units of ϵ, from a time-dependent function to a constant value [Fig. 3(b), top]. When the potential energy does not change, this implies that the shape of the membrane conformation becomes invariant in the rotating field reference frame. This change in the dynamic buckling results in a single Fourier mode for the displacement of the colloids parallel to the precession axis [Fig. 3(b), bottom]. This resembles
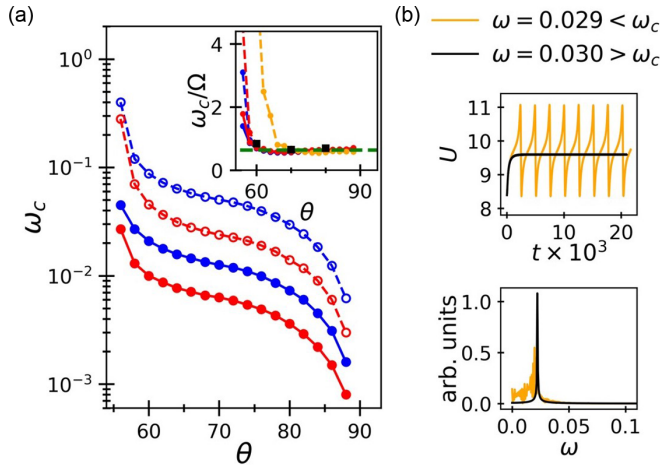
FIG. 3. The synchronous-asynchronous (wobbler-dancer) transition frequency ω_c for a magnetoelastic membrane. (a) MD calculation of ω_c as a function of the field precession angle θ. The solid and dashed lines indicate a dipole magnitude of $\mu = 2$ and $\mu = 1$, respectively. The inset shows the dimensionless transition frequency ω_c/Ω, where Ω is the membrane's characteristic rotation frequency. The green-dashed line represents the theoretical transition at $\omega_c/\Omega = 2/\pi$, which, near $\theta = 90°$, is independent of bending stiffness ($\kappa = 1$, orange. $\kappa = 100$, blue/red). The black squares show the transition calculated from lattice-Boltzmann simulations. (b) Supercritical and subcritical behavior of the total energy U (magnetic + bending) in units of ϵ. The precession frequency is close to the critical frequency, $0.029 < \omega_c < 0.030$ ($\theta = 80°$). Fourier transform of the rotational wave amplitude (bottom).

the transition between the synchronous and the asynchronous motion for oblate magnetic particles [34].

When the precession angle approaches $\pi/2$, the membrane motion becomes independent of the stiffness of the membrane; the membrane remains flat at all times and for all values of ω. As the field precesses, the forces perpendicular to the membrane plane vanish near $\theta = \pi/2$ preventing significant radial bending and, consequently, changing κ does not shift ω_c [Fig. 3(a), inset]. By solving an Euler-Lagrange (EL) equation with Rayleigh dissipation (see Appendix B), we derive an equation of motion for a membrane in a field precessing at a large angle. It reveals a characteristic frequency of membrane motion, $\Omega = 6\zeta(3)\mu_0\mu^2 \sin 2\theta/\pi^2\eta R^2\sigma^4$, where μ_0 is the magnetic permeability of free space, R is the radius of the membrane, η is the viscosity, and $\zeta(x)$ is the Riemann zeta function. The frequency Ω comes from the magnetic ($\propto \mu_0\mu^2 \sin 2\theta R^2/\sigma^5$) and drag ($\propto \eta R^4/\sigma$) potential functions. The ω_c curves in Fig. 3(a) can be scaled by Ω to obtain a dimensionless transition frequency $\omega_c/\Omega = 2/\pi$ [Fig. 3(a), inset]. This number predicts the mode of actuation of a membrane and defines the membrane response time $\tau = \Omega^{-1}$.

III. HYDRODYNAMIC EFFECTS ON "WOBBLING" MEMBRANES

The previous section investigates the broad range of actuating modes accessible to a magnetoelastic membrane. Using an overdamped system, we identify that membrane wobblers display nonreciprocal motion due to waves propagating around

its perimeter. To study wobbler locomotion, we introduce hydrodynamic interactions using the lattice Boltzmann (LB) method [35] to confirm that the dancer-wobbler transition exists in a viscous fluid. We rewrite the EL equation using a hydrodynamic drag term for a disk ($\propto \eta R^3$), which modifies the characteristic frequency $\Omega = 27\zeta(3)\mu_0\mu^2 \sin 2\theta/64\eta R\sigma^5$ (see Appendix B). We will use this definition for Ω hereafter. Both the EL and the LB methods result in the same dimensionless transition ω_c/Ω [Fig. 3(a), black squares].

The LB method reveals the effect of the wobbler's non-reciprocal motion on the surrounding fluid. This technique, which comes from a discretization of the Boltzmann transport equation, reproduces the incompressible Navier-Stokes equation in the macroscopic limit. The LB method calculates the evolution of a discrete-velocity distribution function f_i at each fluid node that fills the simulation box on a square lattice mesh with a spacing of Δx. The surface of the colloids acts as a boundary and is defined by surface nodes that interact with the fluid using the model developed by Peskin [36]. Care must be taken when implementing the LB method with MD because compliant springs can cause translation of the membrane due to in-plane stretching, which is a mechanism observed in systems of a few colloids [37]. See Appendix C for a complete description of the model.

The fluid flow around the membrane is determined by its symmetry and actuation. The wobbling mode circulates fluid around the membrane diameter in a similar manner to spinning disks [38]. However, the wobbler's axis of rotation moves continuously with the field, which produces an additional circulating flow in the x-y plane far above and below the membrane. For a circular membrane, the speed of the flow field possesses the same mirror symmetry as the forces that drive actuation [Fig. 4(a)].

The centrosymmetry of a circular membrane prevents its center of mass from translating. To induce locomotion, we truncate the membrane by removing a circular segment with a sagitta of length h (Fig. 1). We normalize h by the diameter of the circle to define the degree of truncation of the circular membranes as $S = h/2R$. In contrast with the circular membrane case, the shape of the fluid flow in the truncated membrane changes during a single precession period leading to asymmetric flow field that depends on the relative orientation between the field and the truncation cut [Fig. 4(b)].

The amplitude of propagating waves is particularly relevant for predicting the translational [25] or rotational [27] velocity of a membrane. Here the wobble amplitude can be calculated by balancing the magnetic [30] and drag [38] torque in a viscous fluid (see Appendix D). Under small amplitudes for the rotational wave, we obtain the simple relation

$$\frac{A}{R} = \frac{C}{\tau\omega}, \tag{1}$$

where A is the amplitude, and $C = 32/9\pi^2$ [Fig. 5(a)]. In the limit of small deformations, the bending contribution to the torque along the edge is negligible, unless $\kappa \to \infty$. Equation (1) allows us to calculate the maximum flow speed $u_{max} = 4A/(2\pi/\omega)$ from Fig. 4, assuming no-slip boundaries.

The amplitude A is independent of the membrane size since $\tau \propto R$. However, the membrane is not free to increase in radius arbitrarily. The small Re condition implies that
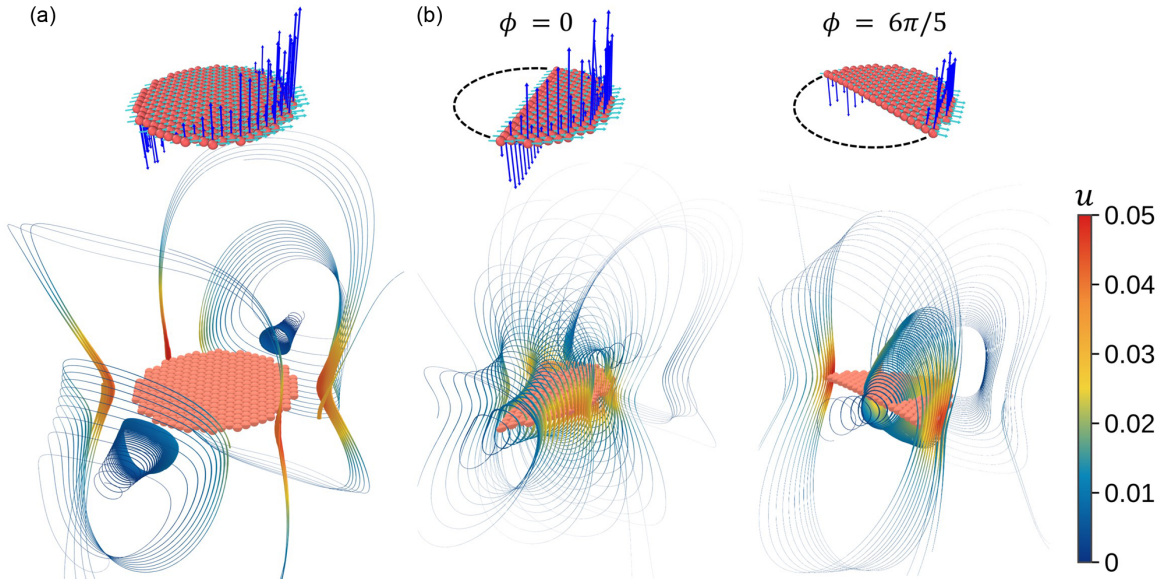
FIG. 4. Fluid flow around a magnetoelastic membranes in the "wobbler" regime. The top images show the total force vector for each colloid (blue arrows) alongside the dipole orientation (cyan arrows) for a precessing field ($\mu = 1$, $\theta = 70°$, $\omega = 0.1$). The bottom images show streamlines around the membrane, where the color indicates flow speed u. (a) A snapshot of a circular membrane. (b) Two snapshots of a truncated circular membrane separated by a shift in the field precession $\Delta\phi = \omega t = 6\pi/5$.

$\nu \gg R^2/\tau$, where ν is the kinematic viscosity. Obeying this constraint on τ, we can define a magnetoviscous parameter $\tau\omega$ and use it to predict locomotion.

Asymmetry in the fluid flow due to $S > 0$ leads to a membrane that travels with a net velocity in the direction of the truncation cut. This net motion is caused by the decrease in the amplitude of the waves traveling along the truncated edge. Since the truncated edge is closer to the center of mass and κ is homogeneous, the membrane will bend to a lesser extent along the truncation. This manifests as a net motion every $2\pi/\omega$, where reversing the handedness of the field reverses the locomotive direction.

While there is a net velocity along the truncation cut, rotation causes the membrane to follow a curved path. This rotation emerges exclusively due to the magnetic interactions perpendicular to the wobbling membrane. If the projection of the forces, visualized in Fig. 4, on the x-y plane is nonzero, the membrane will rotate. This rotation increases as ω approaches ω_c. Torque due to the underlying colloidal lattice is negligible. Over many precession periods, the membrane moves in a circular path around a central point [Fig. 5(b)]. The radius ρ of the path depends on S and A_{avg}. Untruncated $S = 0$ and fully truncated $S = 1$ do not translate and result in $\rho = 0$. Hence a maximum for ρ exists at intermediate S
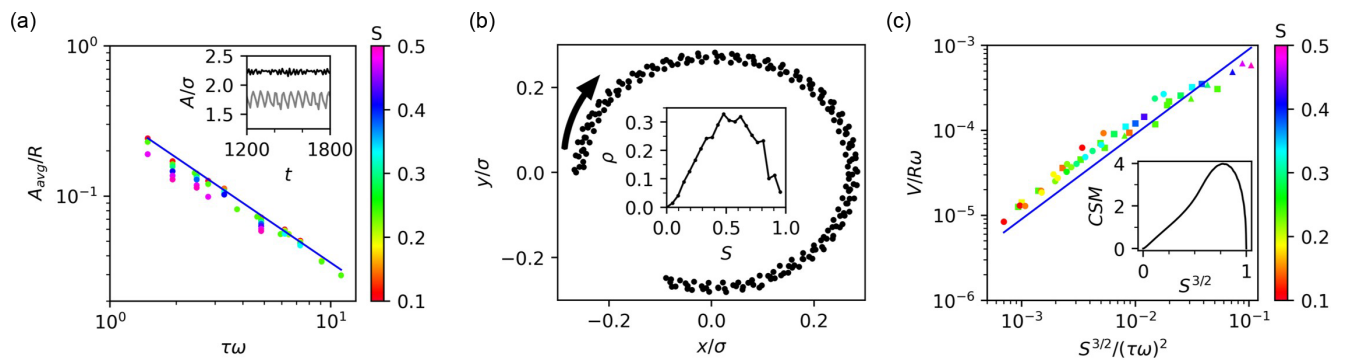

FIG. 5. Actuation drives circular locomotion of truncated magnetoelastic membranes through a viscous fluid. (a) The average rotational ("wobble") wave amplitude A_{avg}, scaled by the membrane radius R, depends inversely on the magnetoviscous parameter $\tau\omega$. Data points from lattice Boltzmann simulations are compared to our analytical model (solid blue line). The coloration of the simulation data notes the degree of truncation S. The inset shows the variation in A/σ over time based on membrane geometry ($S = 0.05$, black; $S = 0.5$, gray), where σ is the colloid diameter. (b) The path taken by a membrane in a precessing field. The arrow indicates the travel direction with velocity V. The inset shows the radius ρ of this path as a function of S. (c) The membrane velocity is proportional to $A_{avg}^2 \propto (\tau\omega)^{-2}$ and scales with $S^{3/2}$ due to changes in the length of the membrane perimeter. The data point shapes are coded by the membrane radius ($R = 7$, triangle; $R = 9$, square; $R = 12$, circle). The blue line shows our analytical prediction (slope $= 1.0$). The inset shows the continuous inversion symmetry measure for a flat truncated membrane.
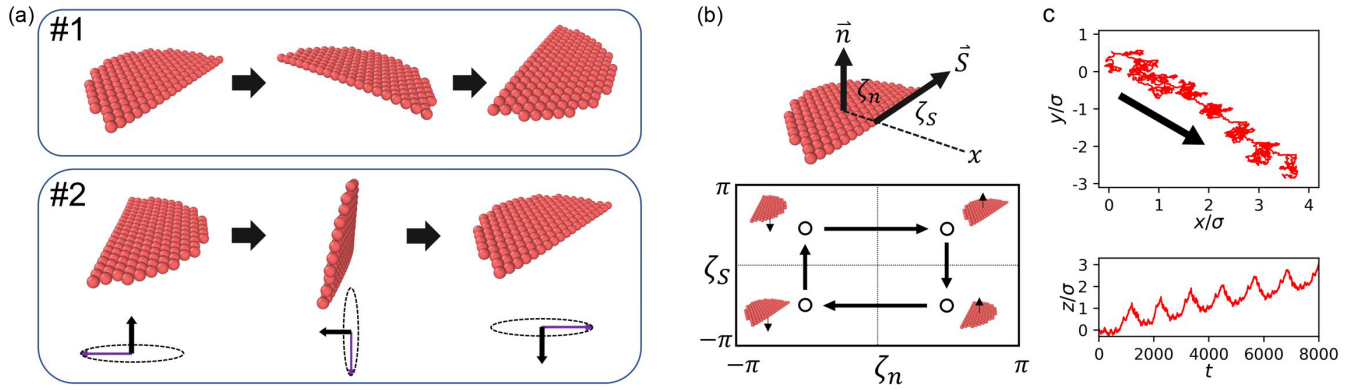
FIG. 6. A two-step magnetic field directs a swimming membrane along a path. (a) First, a membrane wobbler moves under a precessing magnetic field. After it rotates a half turn (#1), the precession switches to a fast frequency at $\theta = \pi/2$ while the axis rotates to flip the membrane (#2). (b) We define the angles that the normal vector $\boldsymbol{n}$ and the truncation vector $\boldsymbol{S}$ make with the x axis as ζ_n and ζ_S, respectively. (c) The path in conformation space over the two-step field. (c) Repeated cycles from (a) move the membrane against the Brownian motion of a thermalized fluid. The upper panel shows the motion of the membrane in the x-y plane. The black arrow indicates the direction of motion. The lower panel shows the displacement in the z direction.

values [Fig. 5(b) inset]. Since the membrane is composed of colloids, irregularities in the $\rho(S, A_{avg})$ curve appear because the symmetry of the membrane changes in discrete steps as subsequent rows of colloids are removed with increasing S. In the limit $\sigma \to 0$, the plot of ρ vs S would become smooth.

The magnetic field controls how quickly the membrane travels along the circular path and affects its angular velocity. Together with the truncation S, the velocity V at which the membrane translates along the path can be determined using a singularity method. With a nearest-neighbor assumption for the magnetic interactions and treating them as point disturbances, the advective flow through the center of mass leads to the velocity

$$\frac{V}{R\omega} = \frac{C^2}{12\zeta(3)} \frac{S^{3/2}}{(\tau\omega)^2}, \tag{2}$$

where the $S^{3/2}$ dependence comes from the number of uncompensated point forces formed by truncation. The velocity is normalized by the phase speed $R\omega$ and is displayed as the blue line in Fig. 5(c). The inverse squared relation on $\tau\omega$ for the velocity is a result of the dependence on the product of the magnetic force and wave amplitude, which in turn relies on the magnetic force. Here we recover the velocity dependence on the square of the wave amplitude [25] but with a lower velocity ($V \leqslant V_{Taylor}/6$). Details of the full derivation are found in Appendix E. We see a deviation between simulations and Eq. (2) at large values of $S^{3/2}/(\tau\omega)^2$ owing to either a high degree of truncation (a linear polymer) or a small viscomagnetic parameter ("dancer"). The direction of travel along the circular path is dictated by the handedness of the precessing field and is an example of magnetically induced symmetry breaking. We find that the continuous symmetry measurement [39] can predict relative changes in the velocity of locomotion. When the inversion asymmetry increases, V increases [Fig. 5(c), inset] because the conformational path taken by the membrane widens, leading to greater net work done on the fluid [40].

IV. MEMBRANE SWIMMING

Here we give an example of how a programmed magnetic field can produce a nonreciprocal conformational path that results linear swimming. In Fig. 6(a), we show that a precessing field can rotate the membrane 180° from its initial configuration. Then, the precession frequency is increased and θ is set to $\pi/2$. This keeps the membrane flat in the precession plane while the precession axis is rotated to flip the membrane. This field is turned on for a period of π/ω_s to flip the membrane orientation, where $\omega_s > \omega$. Once the membrane resembles the starting configuration, the two-step field is repeated. After half the orbit from Fig. 5(b) is obtained, the membrane's center of mass has shifted $\sim 2\rho$. The "flip" from the second field places the membrane back into its original configuration. This recovery stroke moves the membrane back toward its original position, but not entirely, leading to a net translation. The chirality and duration of the magnetic field precession controls the displacement in the membrane plane and the flip direction controls the direction for the out-of-plane displacement. The fastest achievable velocity using this method is $V_{max} = (2/\pi)V$ but will be slowed by the time taken during the recovery step.

This cycle forms a closed loop in configuration space based on two independent degrees of freedom, ζ_n and ζ_S, defined by the angles the normal vector $\boldsymbol{n}$ and the truncation vector $\boldsymbol{S}$ make with the x axis, respectively [Fig. 6(b)]. This configuration loop is an example of nonreciprocal motion, like the wobbling mode but is needed to achieve efficient swimming since the latter only follows circular paths. Thermalizing the LB fluid to 1 $k_B T$, by the method of Adhikari *et al.* [41] for $S^{3/2}/(\tau\omega)^2 \approx 10^{-2}$, shows a swimming membrane as ζ_n and ζ_S changes [Fig. 6(c)]. In this instance, the path during the rotation step, to change ζ_S, is dominated by Brownian motion. The largest displacement occurs during the flipping step to change ζ_n. Additionally, each flip shifts the membrane along the z axis, where the traveling direction is determined by the handedness of the flip. By controlling the precession axis orientation, a membrane may be directed along an arbitrary path.

The useful swimming regime is bound by the Péclet number (Pe) and the dimensionless transition frequency. In other words, the system parameters, in particular the field frequency ω, must be large enough to maintain the wobbling mode but not too large as to attenuate the wobble amplitude below an efficient swimming velocity. In practice, this implies operating at a driving frequency just above ω_c. The range for the frequency can be written as $\omega_c < \omega < C^2 \eta R^3 S^{3/2}/\sqrt{2}\,\zeta(3)\tau^2 k_B T$, where the upper bound is set to Pe = 1. Here we calculate Pe $= VR/D$ using the membrane swimming velocity V, the radius R as the characteristic length, and set the diffusion coefficient D using the radius of gyration of a disk [42]. For example, a membrane of $R = 1$ μm composed of 25 nm magnetite nanoparticles at 25°C in water subject to 50 mT field [43] precessing at 80° gives an effective frequency range of 1–10 kHz.

V. CONCLUSION

Superparamagnetic membranes with homogeneous composition require both nonreciprocal motion and shape asymmetry to swim in viscous fluids. While the Scallop Theorem [20] makes the necessity for nonreciprocal motion known, implementing such motion without modifying the elastic or magnetic homogeneity implies using a "nonreciprocal" magnetic field, where the field vector returns to its starting position without retracing its path. Using a field that does not self-retrace imparts a change in membrane conformation that breaks time-reversal symmetry. However, this type of external magnetic field will still generate centrosymmetric forces within a symmetric membrane. Therefore shape asymmetry is also needed to displace the membrane center of mass during each period of motion, where more asymmetry leads to a larger per-period displacement.

APPENDIX A: THE MD MODEL

We describe a membrane of radius R that is inextensible but can bend in response to a dynamic magnetic field. The membrane is a monolayer of N hexagonally, close-packed magnetic colloids with diameter σ. Membrane flexibility is determined by the quadratic dihedral potentials between each colloid i and three of its nearest neighbors $U_{\text{bend}} = \frac{\kappa}{2}\sum_i^N \sum_j^n \varphi_j^2$, where κ is the bending rigidity, φ_j is the dihedral angle, and n is the number of dihedrals around i. The bending rigidity κ has units of energy and is scaled by the energy unit ϵ.

We model an implicit, uniform magnetic field by constraining the orientation of the colloids' dipole moments in the direction of the field, $\boldsymbol{H} = \boldsymbol{\mu}/\chi$, where χ is the magnetic

susceptibility of the material and $\boldsymbol{\mu}$ is the dipole moment with magnitude μ. The instantaneous dipole orientation is $\hat{\boldsymbol{\mu}} = \sin\theta \sin\omega t\, \hat{\boldsymbol{i}} + \sin\theta \cos\omega t\, \hat{\boldsymbol{j}} + \cos\theta\, \hat{\boldsymbol{k}}$, where θ is the field precession angle, ω is the precession frequency, and t is time. The timescale of the simulation is given in units of $t^* = \sigma\sqrt{m/\epsilon}$, where m is the mass of a colloid. We use the simulation time step $\Delta t = 10^{-3}\, t^*$.

The contribution of the dipole potential energy U_{dipole} to the total energy U is the sum of the dipole-dipole potential energy over all colloids. The dipole-dipole interaction is given by $U_{\text{dipole}} = \sum_i^N \sum_j^{N'} \frac{\mu_0 \mu^2}{4\pi r_{ij}^3}(1 - 3(\hat{\boldsymbol{\mu}} \cdot \hat{\boldsymbol{r}}_{ij})^2)$, where $\hat{\boldsymbol{r}}_{ij}$ is the displacement vector between colloids i and j. The total energy U is scaled by ϵ, and the dipole μ is reported in units of $\sqrt{\mu_0/4\pi\sigma^3\epsilon}$, where μ_0 is the magnetic permeability. The dipole-dipole interaction is cut off for all colloids $r_{ij} > 10\sigma$. Finally, the motion of the colloids are damped by a drag force, $-\xi v(t)$, proportional to the colloid velocity, $v(t)$, and the damping coefficient $\xi = 5 \times 10^2\, m/t^*$.

The dynamic states of the membrane were determined by calculating the total potential energy of the membrane over 10^2 precession periods. The transition frequency was determined to within an error of $\pm 10^{-3}$. The transition was confirmed by taking the Fourier transform of the beads position data over time, $\mathcal{F}[x(t)]$, $\mathcal{F}[y(t)]$, $\mathcal{F}[z(t)]$. The MD simulations were performed using LAMMPS [44] and snapshots of the membrane were visualized using the software OVITO [45].

APPENDIX B: EL APPROACH FOR THE CRITICAL FREQUENCY TRANSITION

We derive the dimensionless transition frequency ω_c/Ω from Fig. 2. A rigid disk of radius R and thickness σ moves in response to a magnetic field. The motion of the disk is synchronous to the field and is visually similar to the rotational wobble of an Euler disk. The disk's orientation is defined by the central normal vector on the face of the disk $\hat{\boldsymbol{n}} = -\sin\gamma \cos\omega t\, \hat{\boldsymbol{i}} + \sin\gamma \sin\omega t\, \hat{\boldsymbol{j}} + \cos\gamma\, \hat{\boldsymbol{k}}$ where γ is the angle of precession around the z axis for $\hat{\boldsymbol{n}}$. We find γ for the steady state by solving the EL equation with a velocity-dependent (Rayleigh) dissipation function [46]. For convenience, we define a second angle $\alpha(t)$ with respect to the x-y plane. This angle is formed by a vector $\hat{\boldsymbol{r}}_x$ that points along the x axis in the disk plane. From the equation for $\hat{\boldsymbol{n}}$, we get the relationship $\alpha(0) = \gamma$. The EL equation for the dynamics of the disk, using the degree of freedom $\alpha(t)$, is written as

$$\frac{d}{dt}\frac{\partial L}{\partial \dot{\alpha}} - \frac{\partial L}{\partial \alpha} + \frac{\partial P}{\partial \dot{\alpha}} = 0, \tag{B1}$$

where $\alpha = \alpha(t)$, $\dot{\alpha} = d\alpha/dt$; P is the dissipation function; and L is the Lagrangian. The Lagrangian is defined as the difference $T - U$, where T is the kinetic energy, and U is the potential energy. Now we can expand Eq. (B1) as

$$\frac{d}{dt}\frac{\partial T}{\partial \dot{\alpha}} - \frac{d}{dt}\frac{\partial U}{\partial \dot{\alpha}} - \frac{\partial T}{\partial \alpha} + \frac{\partial U}{\partial \alpha} + \frac{\partial P}{\partial \alpha} = 0. \tag{B2}$$

Since $\frac{\partial T}{\partial \alpha} = 0$ and angular acceleration is negligible when Re $\ll 1$, we are left with

$$\frac{\partial U}{\partial \alpha} + \frac{\partial P}{\partial \dot{\alpha}} = 0. \tag{B3}$$

We take P as the Rayleigh dissipation function defined as

$$P = \frac{1}{2} \sum_i^N \xi(y\dot{\alpha})^2, \tag{B4}$$

where the sum is over all N colloids i in the disk, y is the distance from the rotation axis and $\xi = 3\pi\eta\sigma$, where η is the dynamic viscosity and σ is the colloid diameter. The sum over all colloids is given by the integral

$$P = \frac{2\xi}{\sigma^2} \int_0^R \int_0^{\sqrt{R^2-x^2}} (y\dot{\alpha})^2 dy dx = \frac{3\pi^2\eta R^4}{4\sigma} \dot{\alpha}^2. \tag{B5}$$

To calculate the total potential energy U, we only need to consider the contribution by the magnetic potential energy. For simplicity, we use a nearest-neighbor approximation on a hexagonal lattice and sum the magnetic interactions over all colloids in the membrane.

$$U = \frac{\mu_0}{4\pi} \frac{\mu^2}{\sigma^3} \sum_i^N \sum_j^n (1 - 3(\hat{\boldsymbol{\mu}} \cdot \hat{\boldsymbol{r}})^2), \tag{B6}$$

where the sum is over each colloid i in the disk of N colloids, for all n nearest neighbors indexed by j, μ_0 is the magnetic permeability of free space, μ is the dipole magnitude, and σ is the nearest-neighbor distance. Each colloid on a hexagonal lattice has a set displacement vectors, $\hat{\boldsymbol{r}}$, that point toward its six nearest neighbors: $\hat{\boldsymbol{r}}_x = \pm(\sqrt{1-C_x^2}, 0, C_x)$, $\hat{\boldsymbol{r}}_{y1} = \pm(\frac{\sqrt{1-C_1^2}}{2}, \frac{\sqrt{3-3C_1^2}}{2}, C_1)$, $\hat{\boldsymbol{r}}_{y2} = \pm(\frac{\sqrt{1-C_2^2}}{2}, -\frac{\sqrt{3-3C_2^2}}{2}, C_2)$, where $C_x = -\tan\alpha$, $C_1 = -(\frac{1}{2} + \frac{\sqrt{3}}{2}\tan\omega t)\tan\alpha$, $C_2 = -(\frac{1}{2} - \frac{\sqrt{3}}{2}\tan\omega t)\tan\alpha$. We ignore a correction for the colloids along the perimeter by assuming $2\pi R/\pi R^2$ is small for large $R \gg \sigma$. Plugging in $\hat{\boldsymbol{\mu}}$ and the displacement vectors $\hat{\boldsymbol{r}}_i$, into Eq. (B6), we expand U in a Taylor series to the first order about the point $\alpha = 0$ (the small wave amplitude regime) to yield

$$U = A_0 + \frac{9R^2\mu_0\mu^2 \sin 2\theta \sin \omega t}{2\sigma^5} \tan\alpha + \mathcal{O}(\alpha^2). \tag{B7}$$

The lower order terms in A_0 are not dependent on α and therefore can be ignored. The accuracy of U can be increased by summing the contribution from dipole-dipole interactions between all colloids. While explicitly adding the contribution from second-nearest neighbors, third and so on is possible, doing so rapidly increases the complexity of U. Since the contribution to the potential energy decreases as $1/r^3$ on a regular lattice $\frac{1}{r^3}(1 + \frac{1}{2^3} + \frac{1}{3^3} + ...)$, the sum can be modified by the Riemann zeta function, $\zeta(3) \approx 1.202$. Therefore to better approximate the full potential, we replace U with $U' = \zeta(3)U$.

Plugging U' and P into Eq. (B3), we obtain

$$\dot{\alpha} + \Omega_l \sec^2\alpha \sin \omega t = 0, \tag{B8}$$

where $\Omega_l = 6\zeta(3)\mu_0\mu^2 \sin 2\theta/\pi^2\sigma^4\eta R^2$ for a system with simple friction on each colloid. For a hydrodynamic system, the potential dissipation function $P = \frac{1}{2}\xi\dot{\beta}^2$ is taken to be consistent with the torque acting on a rotating disk in a viscous fluid, $\xi = \frac{32}{3}\eta R^3$. This changes the size scaling dependence to yield $\Omega_h = 27\zeta(3)\mu_0\mu^2 \sin 2\theta/64\sigma^5\eta R$. The inverse of Ω_h represents the timescale of the membrane's magnetoviscous response $\tau = 1/\Omega_h$ and is part of the magnetoviscous parameter $\tau\omega$. Solving Eq. (B8) for α,

$$\frac{1}{2}\left(\alpha + \frac{\sin 2\alpha}{2}\right) = \frac{\Omega_i}{\omega} \cos \omega t + Z, \tag{B9}$$

where $i = l$ or h, and $Z = 0$ using the boundary condition $\alpha = 0$ at $\omega t = -\pi/2$. The dynamic transition occurs at $\alpha \to \pi/2$ during the maximum possible amplitude over a field precession. During steady-state conditions this occurs at $\omega t = 0$. Doing so leads to a simple relation for the transition frequency

$$\frac{\omega_c}{\Omega} = \frac{2}{\pi}. \tag{B10}$$

APPENDIX C: COUPLING OF LB FLUID TO THE MD MODEL

Hydrodynamic interactions are coupled to the MD model using the LB method [35]. This technique, which comes from a discretization of the Boltzmann transport equation, reproduces the incompressible Navier-Stokes equation in the macroscopic limit. The LB method calculates the evolution of a discrete-velocity distribution function f_i at each fluid node that fills the simulation box on a square lattice mesh with a spacing of Δx. The surface of the colloids act as a boundary and is defined by surface nodes that interact with the fluid using the model developed by Peskin [36].

Using the Bhatnagar-Gross-Krook collision operator [47], the LB equation becomes $f_i(\boldsymbol{x} + \boldsymbol{c}_i\Delta t, t + \Delta t) - f_i(\boldsymbol{x}, t) = -\frac{\Delta t}{\tau}(f_i(\boldsymbol{x}, t) - f_i^{eq}(\boldsymbol{x}, t)) + W_i$. The left-hand side describes the fluid streaming from one node to neighboring nodes along the velocity $\boldsymbol{c}_i$. The first term on the right-hand side describes the relaxation of the distribution f_i to the equilibrium distribution f_i^{eq}, where τ is the relaxation time. The W_i term defines external forces on the fluid. These forces are distributed from nodes that define the surface of the colloids, $\sigma/2$ distance away from the particle center. These nodes interact with the fluid using the immersed boundary model developed by Peskin [36].

The fluid parameters are set to reproduce the frictional coefficient of a spherical colloid, which accurately reproduces the drag on a disk. The disk is immersed within a box of $112 \times 112 \times 113$ nodes. The spacing between nodes was set as $\Delta x = \sigma/2$ while the time step was set to match the MD simulations. Decreasing Reynolds numbers in a LB fluid can be achieved by choosing an increasing the lattice spacing Δx, increasing the time relaxation parameter or decreasing the Mach number, set by the speed of sound $c_s = \frac{1}{\sqrt{3}}\frac{\Delta x}{\Delta t}$ [48]. It is necessary to maintain resolution of the fluid circulation along the membrane edge and avoid numerical errors associated with increasing the relaxation parameter. Therefore we rely on a small time step Δt that also integrates effectively with the harmonic potentials in the MD scheme to maintain Re $\ll 1$.

The "two-step" magnetic field was employed using a truncated membrane ($S = 0.48$). The temperature of the LB fluid was thermalized to $1\,k_B T$ [41]. The first step ran for 21 precession periods with $S^{3/2}/(\tau\omega)^2 = 2\times10^{-2}$. The second step set the precession angle to $\pi/2$ and rotated the precession axis at a frequency $\omega/\omega_s \approx 10$ for roughly 1/3 the duration of the first step. Because the wobbling mode is stable, the flip does not need to lie perfectly in the x-y plane for the process to repeat effectively.

APPENDIX D: DERIVATION OF THE MAGNETOVISCOUS PARAMETER $\tau\omega$

The magnetoviscous parameter is found by considering a magnetoelastic membrane in the small amplitude limit. Under small distortions, the bending and stretching forces can be neglected. However, the flexibility of the membrane means that only a small area δa near the perimeter is in motion. Therefore we consider Eq. (B3) over δa moving freely along the z direction. We write the drag as simply $\frac{\partial P}{\partial z} = 3\pi\eta\sigma\dot{z}\delta a$. Solving for the resulting first-order differential equation yields

$$\frac{z}{R} = \frac{C\cos\omega t}{\tau\omega}, \tag{D1}$$

where the equation is put in terms of $\tau = 1/\Omega$, and $C = 32/9\pi^2$. The amplitude is maximized $z_{\max} = A$ when $\cos\omega t = 1$, From this equation, we see that the reduced amplitude of the rotational waves is inversely proportional to the magnetoviscous parameter.

APPENDIX E: SINGULARITY METHOD FOR MEMBRANE ADVECTION

We use a singularity method to determine the advection of the membrane in a viscous fluid due to point forces generated by magnetic dipole interactions. The fluid velocity at $\boldsymbol{x}$ is calculated by summing over all point disturbances [49]

$$\boldsymbol{v}(\boldsymbol{x}) = \frac{1}{8\pi\eta}\int \boldsymbol{G}(\boldsymbol{x}-\boldsymbol{y})\cdot\boldsymbol{f}(\boldsymbol{y})d\boldsymbol{y}, \tag{E1}$$

where η is the dynamic viscosity, $\boldsymbol{f}(\boldsymbol{y})$ is a point force located at $\boldsymbol{y}$, $\boldsymbol{G}(\boldsymbol{r}) = \frac{\boldsymbol{I}}{|r|} + \frac{\boldsymbol{r}\boldsymbol{r}}{|r|^3}$ is the Oseen tensor, and $\boldsymbol{I}$ is the identity matrix.

At every point on the membrane surface, the no-slip fluid velocity is related to the rigid translation $\boldsymbol{V}$ and angular rotation $\boldsymbol{W}$ by

$$\boldsymbol{v}(\boldsymbol{x}) = \boldsymbol{V} + \boldsymbol{W}(\boldsymbol{x}-\boldsymbol{x}_{\text{com}}), \tag{E2}$$

where $\boldsymbol{x}_{\text{com}}$ is the initial center of mass located at the origin. Since we are interested in the center of mass advection $\boldsymbol{v}(\boldsymbol{x}_{\text{com}})$, we can ignore the rotation $\boldsymbol{W}$ of the membrane and solve Eq. (E1) to obtain $\boldsymbol{V}$.

Equation (E1) can be simplified by considering the underlying lattice and membrane symmetry. For colloids arranged in a lattice along a rigid disk, the magnetic dipole force cancels out for all colloids in the bulk. Therefore the forces along the perimeter dominate. Furthermore, the center of inversion symmetry for all points along the perimeter of a circular membrane yields opposite forces of equal distance from the center resulting in no locomotion, $\boldsymbol{v}(\boldsymbol{x}_{\text{com}}) = 0$. Therefore we create an imbalance of point forces by making a small truncation along the y direction in the $x > 0$ domain (i.e., we remove a circular segment centered on the x axis). The difference in the number of point forces due to truncation ΔN on opposite sides of the membrane is due to the number of colloids that can fit along the difference in the edge lengths $\Delta L/\sigma$, where $\Delta L = 2R[2\sqrt{S(1-S)} - \sin^{-1}(2\sqrt{S(1-S)})]$. By using the Puiseux series, we can approximate $\Delta N = 8RS^{3/2}/3\sigma$, which is accurate for $S < (3/8)^{2/3} \approx 0.52$. Since the truncation is small, the point force imbalance occurs along the vector $\boldsymbol{x} = -R\hat{\boldsymbol{r}}_x$. We calculate $\boldsymbol{V} = \boldsymbol{v}(\boldsymbol{x}_{\text{com}})$ for an infinitesimally thin disk. With these simplifications, Eq. (E1) and takes the form

$$\boldsymbol{V} = \frac{\Delta N(\hat{\boldsymbol{\mu}}\cdot\hat{\boldsymbol{r}}_x)}{8\pi\eta R}(\boldsymbol{I}+\hat{\boldsymbol{r}}_x\hat{\boldsymbol{r}}_x)\cdot\hat{\boldsymbol{\mu}}. \tag{E3}$$

Time-averaging $\boldsymbol{v}$ over the precession period $2\pi/\omega$, we obtain

$$\langle V_x\rangle = \langle V_z\rangle = 0 \tag{E4}$$

$$\langle V_y\rangle = \frac{S^{3/2}\mu_0\mu^2\sin 2\theta\tan\gamma}{8\pi^2\eta\sigma^5} \tag{E5}$$

and see that the membrane velocity V is directed along the truncation cut. We can replace the reduced amplitude $\tan\gamma$ with the previous definition of the magnetoelastic parameter to obtain a nondimensional swimming velocity reduced by $R\omega$,

$$\frac{V}{R\omega} = \frac{C^2}{12\zeta(3)}\frac{S^{3/2}}{(\tau\omega)^2}. \tag{E6}$$

For the two-step linear swimmer, the theoretical maximum swimming speed, assuming no distance loss during the recovery stroke, is the path the membrane follows around consecutive semicircles, $V_{\max} = \frac{2}{\pi}\langle V_y\rangle$.

[1] T. Dombrowski and D. Klotsa, Kinematics of a simple reciprocal model swimmer at intermediate reynolds numbers, Phys. Rev. Fluids **5**, 063103 (2020).

[2] R. Dreyfus, J. Baudry, M. Roper, M. Fermigier, H. Stone, and J. Bibette, Microscopic artificial swimmers, Nature (London) **437**, 862 (2005).

[3] B. Jang, E. Gutman, N. Stucki, B. F. Seitz, P. D. Wendel-García, T. Newton, J. Pokki, O. Ergeneman, S. Pané, Y. Or, and B. J. Nelson, Undulatory locomotion of magnetic multilink nanoswimmers, Nano Lett. **15**, 4829 (2015).

[4] M. T. Bryan, J. Garcia-Torres, E. L. Martin, J. K. Hamilton, C. Calero, P. G. Petrov, C. P. Winlove, I. Pagonabarraga, P. Tierno, F. Sagués, and F. Y. Ogrin, Microscale Magneto-Elastic Composite Swimmers at the Air-Water and Water-Solid Interfaces Under a Uniaxial Field, Phys. Rev. Applied **11**, 044019 (2019).

[5] C. P. Moerland, L. J. van IJzendoorn, and M. W. J. Prins, Rotating magnetic particles for lab-on-chip applications – a comprehensive review, Lab Chip **19**, 919 (2019).

[6] C. Goubault, P. Jop, M. Fermigier, J. Baudry, E. Bertrand, and J. Bibette, Flexible Magnetic Filaments As Micromechanical Sensors, Phys. Rev. Lett. **91**, 260802 (2003).

[7] S. L. Biswal and A. P. Gast, Mechanics of semiflexible chains formed by poly(ethylene glycol)-linked paramagnetic particles, Phys. Rev. E **68**, 021402 (2003).

[8] S. L. Biswal and A. P. Gast, Micromixing with linked chains of paramagnetic particles, Anal. Chem. **76**, 6448 (2004).

[9] W. Zhu, J. Li, Y. J. Leong, I. Rozen, X. Qu, R. Dong, Z. Wu, W. Gao, P. H. Chung, J. Wang, and S. Chen, 3d-printed artificial microfish, Adv. Mater. **27**, 4411 (2015).

[10] Z. Wu, T. Li, W. Gao, T. Xu, B. Jurado-Sánchez, J. Li, W. Gao, Q. He, L. Zhang, and J. Wang, Cell-membrane-coated synthetic nanomotors for effective biodetoxification, Adv. Funct. Mater. **25**, 3881 (2015).

[11] S. Wu, W. Hu, Q. Ze, M. Sitti, and R. Zhao, Multifunctional magnetic soft composites: a review, Multifunct. Mater. **3**, 042003 (2020).

[12] J. Vyskočil, C. C. Mayorga-Martinez, E. Jablonská, F. Novotný, T. Ruml, and M. Pumera, Cancer cells microsurgery via asymmetric bent surface Au/Ag/Ni microrobotic scalpels through a transversal rotating magnetic field, ACS Nano **14**, 8247 (2020).

[13] H. Markides, M. Rotherham, and A. Haj, Biocompatibility and toxicity of magnetic nanoparticles in regenerative medicine, J. Nanomater. **2012**, 13 (2012).

[14] J. M. Dempster, P. Vázquez-Montejo, and M. Olvera de la Cruz, Contractile actuation and dynamical gel assembly of paramagnetic filaments in fast precessing fields, Phys. Rev. E **95**, 052606 (2017).

[15] P. Vázquez-Montejo and M. O. de la Cruz, Flexible paramagnetic membranes in fast precessing fields, Phys. Rev. E **98**, 032603 (2018).

[16] C. A. Brisbois, M. Tasinkevych, P. Vàzquez-Montejo, and M. O. de la Cruz, Actuation of magnetoelastic membranes in precessing magnetic fields, Proc. Natl. Acad. Sci. USA **116**, 2500 (2019).

[17] Y. Li, G. Huang, X. Zhang, B. Li, Y. Chen, T. Lu, T. J. Lu, and F. Xu, Magnetic hydrogels and their potential biomedical applications, Adv. Funct. Mater. **23**, 660 (2013).

[18] W. Hu, G. Lum, M. Mastrangeli, and M. Sitti, Small-scale soft-bodied robot with multimodal locomotion, Nature (London) **554**, 81 (2018).

[19] C. Li, G. C. Lau, H. Yuan, A. Aggarwal, V. L. Dominguez, S. Liu, H. Sai, L. C. Palmer, N. A. Sather, T. J. Pearson, D. E. Freedman, P. K. Amiri, M. O. de la Cruz, and S. I. Stupp, Fast and programmable locomotion of hydrogel-metal hybrids under light and magnetic fields, Sci. Robot. **5**, eabb9822 (2020).

[20] E. M. Purcell, Life at low Reynolds number, Am. J. Phys. **45**, 3 (1977).

[21] M. Roper, R. Dreyfus, J. Baudry, M. Fermigier, J. Bibette, and H. A. Stone, Do magnetic micro-swimmers move like eukaryotic cells?, Proc. R. Soc. Lond. A **464**, 877 (2008).

[22] T. Yang, B. Sprinkle, Y. Guo, J. Qian, D. Hua, A. Donev, D. W. M. Marr, and N. Wu, Reconfigurable microbots folded from simple colloidal chains, Proc. Natl. Acad. Sci. USA **117**, 18186 (2020).

[23] A. Cebers, Flexible magnetic swimmer, Magnetohydrodynamics **41**, 63 (2005).

[24] M. Arroyo, L. Heltai, D. Millán, and A. DeSimone, Reverse engineering the euglenoid movement, Proc. Natl. Acad. Sci. USA **109**, 17874 (2012).

[25] G. I. Taylor, Analysis of the swimming of microscopic organisms, Proc. R. Soc. Lond. A **209**, 447 (1951).

[26] E. Lauga and T. R. Powers, The hydrodynamics of swimming microorganisms, Rep. Prog. Phys. **72**, 096601 (2009).

[27] G. Corsi, A. De Simone, C. Maurini, and S. Vidoli, A neutrally stable shell in a stokes flow: a rotational taylor's sheet, Proc. R. Soc. Lond. A **475**, 20190178 (2019).

[28] See Supplemental Material at http://link.aps.org/supplemental/10.1103/PhysRevResearch.4.023166 for magnetoelastic membrane with stiffness $\kappa = 10$ under a magnetic field, $\mu = 1.5$, $\theta = 70°$, and $\omega = 0.06$. The coloration highlights the displacement in the z direction. See Video 1.

[29] M. X. Lim, B. VanSaders, A. Souslov, and H. M. Jaeger, Mechanical Properties of Acoustically Levitated Granular Rafts, Phys. Rev. X **12**, 021017 (2022).

[30] K. W. Yung, P. B. Landecker, and D. D. Villani, An analytic solution for the force between two magnetic dipoles, Magn. Electr. Separ. **9**, 39 (1998).

[31] S. S. Park, Z. J. Urbach, C. A. Brisbois, K. A. Parker, B. E. Partridge, T. Oh, V. P. Dravid, M. Olvera de la Cruz, and C. A. Mirkin, DNA- and field-mediated assembly of magnetic nanoparticles into high-aspect ratio crystals, Adv. Mater. **32**, 1906626 (2020).

[32] R. Messina, S. Aljawhari, L. Bécu, J. Schockmel, G. Lumay, and N. Vandewalle, Quantitatively mimicking wet colloidal suspensions with dry granular media, Sci. Rep. **5**, 10348 (2015).

[33] See Supplemental Material at http://link.aps.org/supplemental/10.1103/PhysRevResearch.4.023166 for magnetoelastic membrane with stiffness $\kappa = 20$ under a magnetic field, $\mu = 1.5$, $\theta = 60°$ and $\omega = 0.013$. The coloration highlights the displacement in the z-direction. See Video 2.

[34] J. Cīmurs and A. Cēbers, Dynamics of anisotropic superparamagnetic particles in a precessing magnetic field, Phys. Rev. E **87**, 062318 (2013).

[35] F. Mackay, S. Ollila, and C. Denniston, Hydrodynamic forces implemented into LAMMPS through a lattice-Boltzmann fluid, Comput. Phys. Commun. **184**, 2021 (2013).

[36] C. S. Peskin, The immersed boundary method, Acta. Numer. **11**, 479 (2002).

[37] G. Grosjean, M. Hubert, Y. Collard, S. Pillitteri, and N. Vandewalle, Surface swimmers, harnessing the interface to self-propel, Eur. Phys. J. E **41**, 137 (2018).

[38] J. P. Tanzosh and H. A. Stone, A general approach for analyzing the arbitrary motion of a circular disk in a stokes flow, Chem. Eng. Commun. **148-150**, 333 (1996).

[39] H. Zabrodsky, S. Peleg, and D. Avnir, Continuous symmetry measures, J. Am. Chem. Soc. **114**, 7843 (1992).

[40] G. Grosjean, M. Hubert, G. Lagubeau, and N. Vandewalle, Realization of the Najafi-Golestanian microswimmer, Phys. Rev. E **94**, 021101(R) (2016).

[41] R. Adhikari, K. Stratford, M. E. Cates, and A. J. Wagner, Fluctuating lattice Boltzmann, Europhys. Lett. **71**, 473 (2005).

[42] F. Capuani, I. Pagonabarraga, and D. Frenkel, Lattice-Boltzmann simulation of the sedimentation of charged disks, J. Chem. Phys. **124**, 124903 (2006).

[43] D. Susan-Resiga, V. Socoliuc, A. Bunge, R. Turcu, and L. Vékás, From high colloidal stability ferrofluids to magnetorheological fluids: tuning the flow behavior by magnetite nanoclusters, Smart Mater. Struct. **28**, 115014 (2019).

[44] S. Plimpton, Fast parallel algorithms for short-range molecular dynamics, J. Comput. Phys. **117**, 1 (1995).

[45] A. Stukowski, Visualization and analysis of atomistic simulation data with OVITO-the open visualization tool, Model. Simul. Mater. Sci. Eng. **18**, 015012 (2010).

[46] H. Goldstein, in *Classical Mechanics*, 3rd ed. (Addison-Wesley, Reading, MA, 2000), p. 24.

[47] P. L. Bhatnagar, E. P. Gross, and M. Krook, A model for collision processes in gases. I. small amplitude processes in charged and neutral one-component systems, Phys. Rev. **94**, 511 (1954).

[48] T. Krüger, H. Kusumaatmaja, A. Kuzmin, O. Shardt, G. Silva, and E. M. Viggen, *The Lattice Boltzmann Method—Principles and Practice* (Springer International Publishing, Switzerland, 2017).

[49] E. Guazzelli, J. F. Morris, and S. Pic, *A Physical Introduction to Suspension Dynamics*, Cambridge Texts in Applied Mathematics (Cambridge University Press, Cambridge, England, 2011).